ADVANCED ENGINEERING MATERIALS
www.aem-journal.com

Toward Maximum Utilization of Heavy Rare Earths in Sintered Nd–Fe–B Magnets by Grain Boundary Diffusion Source and Application Area Optimization

Abdullatif Durgun, Dominik Ohmer, Matthias Katter, Andreas Thul, Simon Steentjes, Hossein Sepehri Amin, Oliver Gutfleisch, and Imants Dirba**

Reduction in the utilization of resource critical heavy rare earth (HRE) elements such as Dy and Tb in NdFeB-based magnets is crucial for cost-effective coercivity enhancement at the high operating temperature in E-motors. The grain boundary diffusion process (GBDP) is optimized and aim to maximize HRE utilization by selective magnetic hardening of areas in the magnet such as corners or edges that are highly susceptible to demagnetization, as demonstrated by finite element magnetostatics simulation on an internal permanent magnet synchronous traction motor for electric vehicles. This becomes especially important considering the advent of additive manufacturing, which has the potential to realize such tailored approaches with local magnetic hardening based on specific application requirements. Commonly industrially used HRE source TbH_x, as well as complex multi-component Tb-containing alloys such as $Tb_{10}Pr_{60}(Cu,Al,Ga)_{30}$ are investigated on commercial grade NdFeB-based sintered magnets. Highly efficient Tb utilization with a normalized coercivity increase of 3866 kA/m/wt% Tb (4.86 T/wt% Tb) is achieved with only a minor reduction in remanence from around 1.45 T in the initial magnet to 1.43 T after GBDP, paving the way toward HRE-balanced high-performance magnets for sustainable electric motor applications.

1. Introduction

Reduction in usage of heavy rare earth (HRE) elements for coercivity enhancement in NdFeB-based magnets has been in the research focus for the permanent magnet community during the last decade.[1–5] First-generation magnets were produced by direct HRE alloying[6,7] resulting in a significant reduction in remanence and high HRE consumption. The second generation utilizes the HREs more effectively, hardening only the outer shells of the grains via the grain boundary diffusion process (GBDP),[8–14] the two-alloy,[15,16] HRE powder addition,[17,18] or dual-main-phase approaches.[19–26] This results in preserved remanence and lower HRE consumption. Here, we investigate a third concept–further HRE reduction by strategic selective hardening of areas in the magnet that are most susceptible to demagnetization. Using finite element magnetostatics simulation on an internal permanent magnet synchronous traction motor we aim to identify the areas in a Nd–Fe–B permanent magnet that are most highly susceptible to demagnetization. GBDP optimization is carried out to find the best diffusion source composition and particle size. Furthermore, we demonstrate that HRE utilization can be maximized by strategic local coercivity enhancement in areas in the magnet, such as corners or edges, that are experiencing the highest demagnetization fields in the actual motor applications.

A. Durgun, O. Gutfleisch, I. Dirba
Functional Materials, Institute of Materials Science
Technical University of Darmstadt
64287 Darmstadt, Germany
E-mail: abdullatif.durgun@tu-darmstadt.de;
imants.dirba@tu-darmstadt.de

The ORCID identification number(s) for the author(s) of this article can be found under https://doi.org/10.1002/adem.202501145.

DOI: 10.1002/adem.202501145

D. Ohmer, M. Katter
Vacuumschmelze GmbH & Co. KG
63412 Hanau, Germany

A. Thul, S. Steentjes
Institute of Electrical Machines (IEM)
RWTH Aachen University
52062 Aachen, Germany

H. S. Amin
National Institute for Materials Science
Tsukuba 305-0047, Japan

2. Results and Discussion

2.1. Grain Boundary Diffusion Process Alloy Optimization

First task toward maximum utilization of HREs is to identify the most effective HRE source. Initially, we had chosen to compare different materials reported in the literature quantitatively by calculating the respective coercivity enhancements per amount of HRE, i.e., in units of kA/m/wt% HRE (or alternatively T/wt% HRE). In our opinion, this is the best merit since comparing only the final coercivities can be misleading due to different starting values and the amount of HRE also needs to be implemented because H_c will increase with HRE content, as clearly demonstrated later in the manuscript. A large amount of data on the GBDP for rare earth permanent magnets has been summarized in the review article by Liu et al.[27] which is particularly useful for this task. Unfortunately, a lot of articles report only the coercivity enhancement without mentioning the actual HRE amount and therefore could not be used for this comparison. We suggest that this should change in the future, since in magnet manufacturing, the total mass of HRE used is the number that matters instead of HRE concentration measured locally on a selected area of the sample using an electron microscope. Consequently, we had to find an alternative way for comparing the various HRE sources used and the results are summarized in **Figure 1**a where the coercivity enhancements are plotted as a function of HRE or light rare earth (LRE) wt% in the GBDP source. We have chosen to distinguish between Dy and Tb as HRE sources as well as between various Nd–Fe–B magnet manufacturing routes (HDDR, sintering, melt-spun) since they lead to different microstructures and therefore a direct comparison of the resultant HRE utilization could be misleading. First, on the far-right side in Figure 1a, simple elements (Dy, Tb), and conventionally used binary hydrides/fluorides (e.g., DyH_3, TbH_3)[10,28–34] followed by binary low-melting alloys (e.g., $Tb_{70}Cu_{30}$, $Dy_{70}Cu_{30}$)[35–37] and LRE-based diffusion sources such as $Nd_{70}Cu_{30}$, $N_{80}Ga_{15}Cu_5$, or $Nd_{90}Al_{10}$[16,38–41] are plotted. On the left side, results from complex quaternary and quinary HRE-containing alloys such as Tb–Pr–Cu–Al–Ga[37,42–45] are shown. Two main conclusions are drawn from surveying the literature: 1) the highest absolute coercivity enhancements are reported for diffusion of pure metals or binary hydrides/fluorides; 2) the lowest HRE concentrations are achieved by using complex quaternary and quinary GBDP alloys. Therefore, to identify the most effective and sustainable diffusion sources that minimize the use of critical rare earth elements Dy and Tb, the coercivity enhancement needs to be normalized with respect to the HRE amount. The results in Figure 1b show that the complex quaternary and quinary compositions clearly stand out with the highest coercivity enhancement observed for $Tb_{10}Pr_{60}(Cu,Al,Ga)_{30}$.[42] Therefore, these were chosen for the GBDP studies conducted in the present work.

GBDP source alloy optimization was carried out to find the best composition and particle size. GBDP with application of the source alloy on top and bottom planes perpendicular to the easy axis of a sintered magnet sample with a right parallelepiped shape was systematically investigated. A source alloy ingot directly after induction melting was crushed into a powder and sieved to different particle size fractions (0–63; 80–163; 163–250 μm). Results were compared with ribbons obtained after a subsequent melt spinning. **Figure 2**a shows that coercivity increases consistently with powder particle size, reaching the highest value in the case of direct application of melt-spun ribbons without additional grinding. The reason for this behavior is the high affinity of RE-based alloys toward oxygen, which leads to more oxidation with increasing surface area (smaller particle size) even though powderizing was done inside an Ar-filled glovebox. However, to investigate this effect in more detail, oxygen pickup across the different processing steps would need to be quantified. Accordingly, melt-spun ribbons were chosen for the further experiments in this work. Next, compositional optimization was done for Tb- and Dy-based alloys with the resultant hysteresis loops shown in Figure 2b. As expected, Tb-based alloys outperform Dy-based ones due to the much higher anisotropy field (17.5 MA m^{-1} vs 11.9 MA m^{-1}) of the $Tb_2Fe_{14}B$ phase compared to $Dy_2Fe_{14}B$.[46] The best magnetic properties were achieved for $Tb_{10}Pr_{60}(Cu,Al,Ga)_{30}$ ($Tb_{13.65}Pr_{72.59}Cu_{5.46}Al_{2.32}Ga_{5.99}$ in wt%), most likely due to the higher Pr content compared to higher Cu, Al, Ga in the

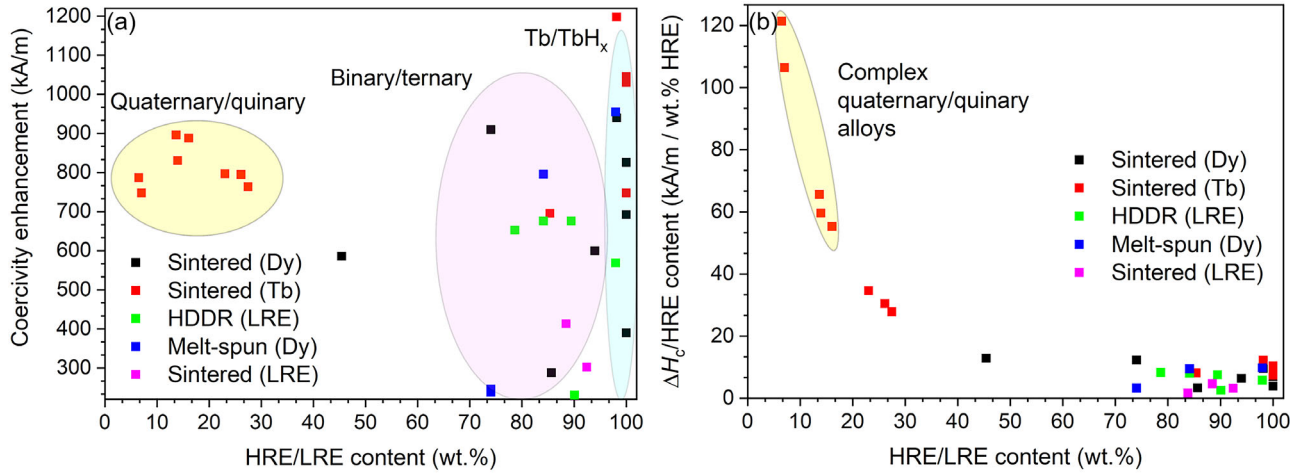

Figure 1. a) Selected literature values for coercivity enhancement by HRE/LRE diffusion in various types of NdFeB magnets. b) The corresponding coercivity enhancement normalized to the RE content showing the efficiency of the different sources.

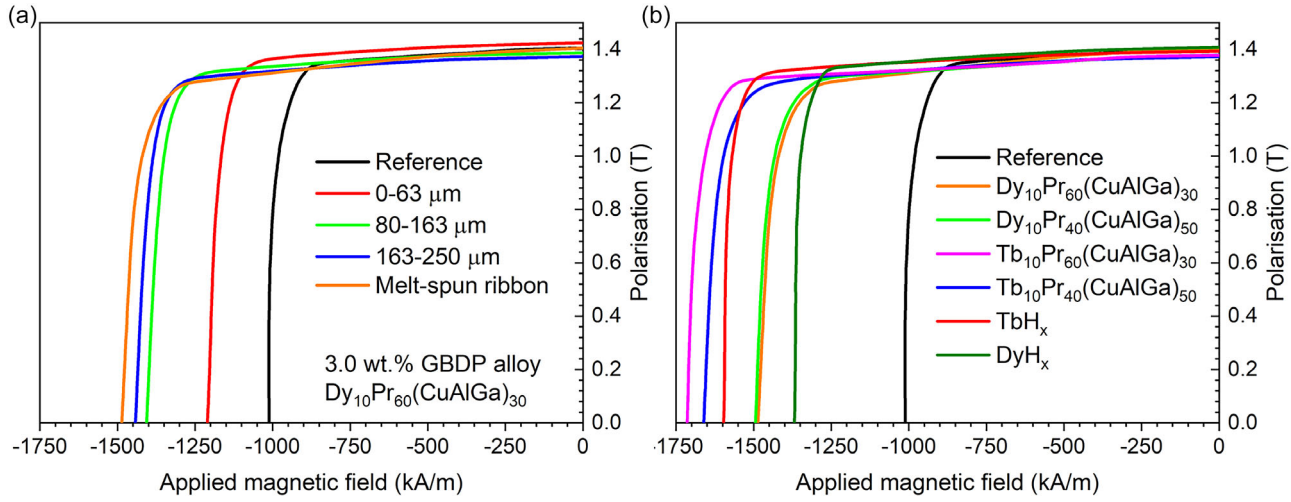

Figure 2. Optimization of GBDP source alloy composition and application form. a) the effect of particle size and b) the effect of composition. 3.0 wt% of GBDP alloy (melt-spun ribbons) and 0.4 wt% HRE hydrides (powder) were used for equal HRE usage.

$Tb_{10}Pr_{40}(Cu,Al,Ga)_{50}$ composition. The exact chemical composition measured by inductively coupled plasma optical emission spectroscopy (ICP-OES) is $Tb_{13.81}Pr_{72.40}Cu_{5.57}Al_{2.52}Ga_{5.70}$ (in wt%) as given in Table S2, Supporting Information. The difference is even more pronounced when the quinary GBDP alloys are compared to conventionally used TbH_x and DyH_x. The weight of all applied materials was calculated to ensure similar HRE usage. Since $Tb_{10}Pr_{60}(Cu,Al,Ga)_{30}$ contains 13.65% Tb, which equals 0.4 wt%, this amount was used in the case of the binary hydrides. TbH_x and DyH_x result in coercivity enhancement ΔH_c of 568 and 348 kA m^{-1}, respectively compared to 701 kA m^{-1} for $Tb_{10}Pr_{60}(Cu,Al,Ga)_{30}$ using the same HRE content. Therefore, this composition was chosen for further studies in this work.

To investigate the melting behavior during the GBDP process, differential thermal analysis (DTA) measurements were done up to 900 °C. DTA heating curve for $Tb_{10}Pr_{60}(Cu,Al,Ga)_{30}$ alloy in **Figure 3**a reveals multiple endothermic melting events with main peaks at 468 and 485 °C which is close to the second GBDP annealing temperature of 500 °C. Scanning electron microscope (SEM) backscattered electron (BSE) image in Figure 3b shows large grains separated by fine two-phase eutectic intercellular mixture for the as-cast alloy. Chemical compositions (atomic %) determined by energy dispersive x-ray spectroscopy (EDX) are $Tb_{8.1}Pr_{56.8}Cu_{2.4}Al_{18.6}Ga_{14.0}$ for the gray matrix phase and $Tb_{4.7}Pr_{39.8}Cu_9Al_{3.1}Ga_{1.1}O_{42.4}$ for the fine dark regions. Oxygen in the Pr-rich phase originates from SEM sample preparation since conventional polishing wheel in ambient atmosphere was used for surface preparation. X-ray diffraction measurement was conducted on the melt-spun ribbons as an attempt to identify the phases and match with the available phase diagrams. The diffractogram is shown in Figure S1, Supporting

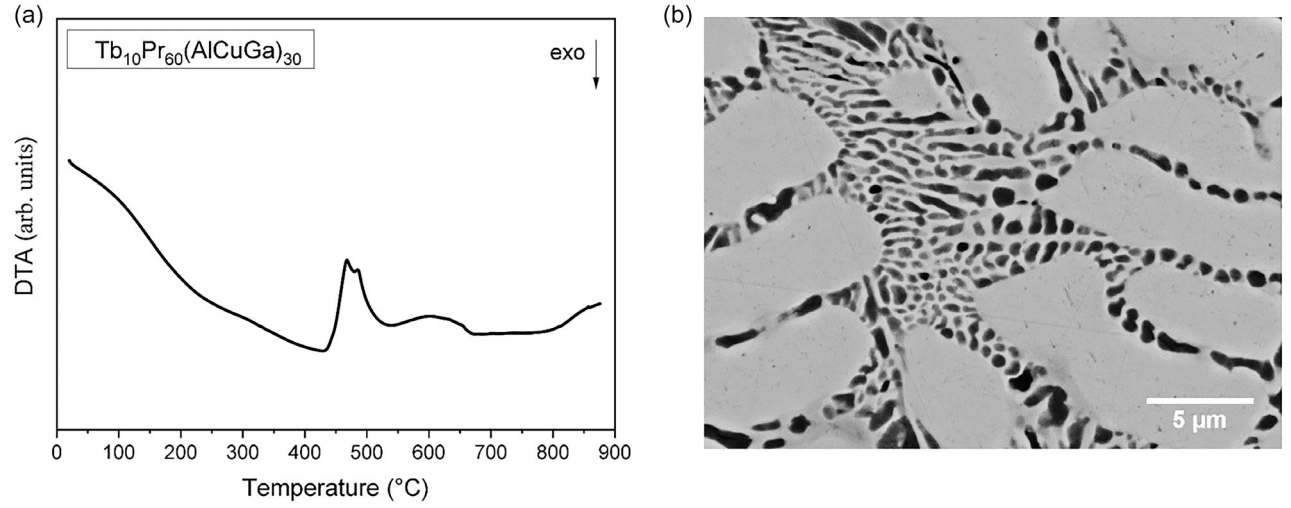

Figure 3. a) DTA heating curve for $Tb_{10}Pr_{60}(Cu,Al,Ga)_{30}$ composition showing multiple endothermic melting events. b) SEM BSE image of the eutectic microstructure for the as-cast alloy.

Information. Due to the high quenching rate of the alloy during melt spinning, no clear crystalline diffraction peaks could be distinguished and therefore phase identification was not possible. Considering the importance of the grain boundary magnetism, melting point and wettability in coercivity development, these results illustrate the potential in search for optimum multicomponent alloys at/near eutectic compositions with suitable properties using computational methods, since for simple binary and ternary alloys equilibrium phase diagrams can be found in handbooks which is not the case for higher order (e.g., quinary) constituent systems.

2.2. Grain Boundary Diffusion Process Optimal HRE Application Amount

As next, a study was conducted to investigate the optimal HRE application amount. 0.3–3.0 wt% of the magnet mass $Tb_{10}Pr_{60}(Cu,Al,Ga)_{30}$ melt-spun ribbons corresponding to 0.041–0.408 wt% Tb, respectively were applied on top and bottom *c*-planes of the samples. As expected, coercivity increases with the applied HRE amount from 1010 kA m^{-1} in the initial magnet to 1710 kA m^{-1} after 3.0 wt% GBDP alloy (0.408 wt% Tb) diffusion treatment, as shown in **Figure 4**a.

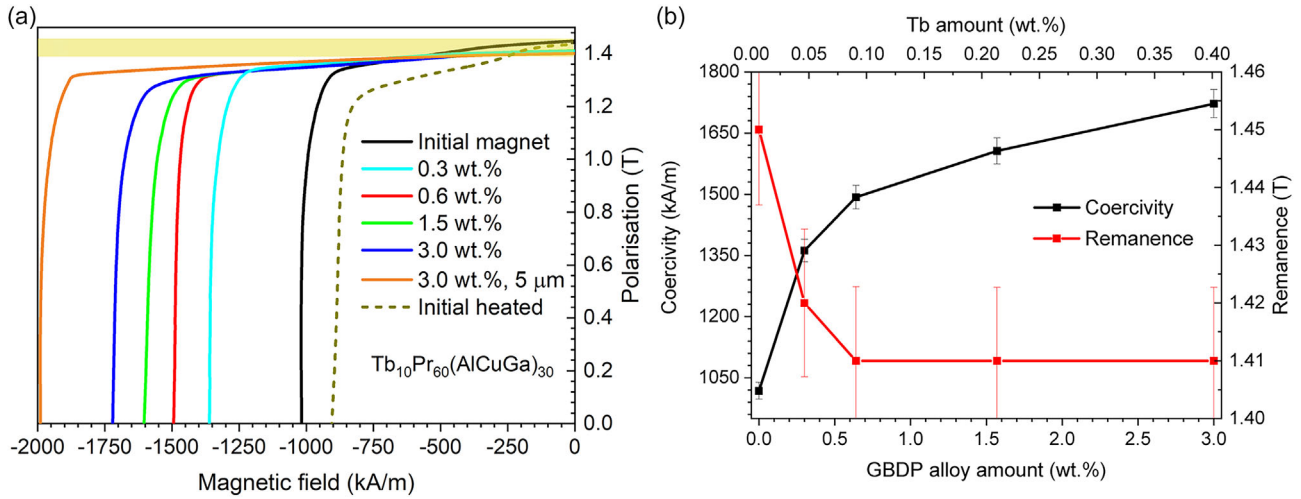

Figure 4. Demagnetization curves a) and summary of the resultant remanence and coercivity values, b) after GBDP with 0.3–3.0 wt% $Tb_{10}Pr_{60}(Cu,Al,Ga)_{30}$ melt-spun ribbons corresponding to 0.041–0.408 wt% Tb applied on top and bottom *c*-planes as illustrated in the inset. The shaded area in (a) indicates the statistical deviation in remanence of the initial commercial sintered magnet samples. The dashed line represents blank initial magnet exposed to the same heat treatment as a reference.

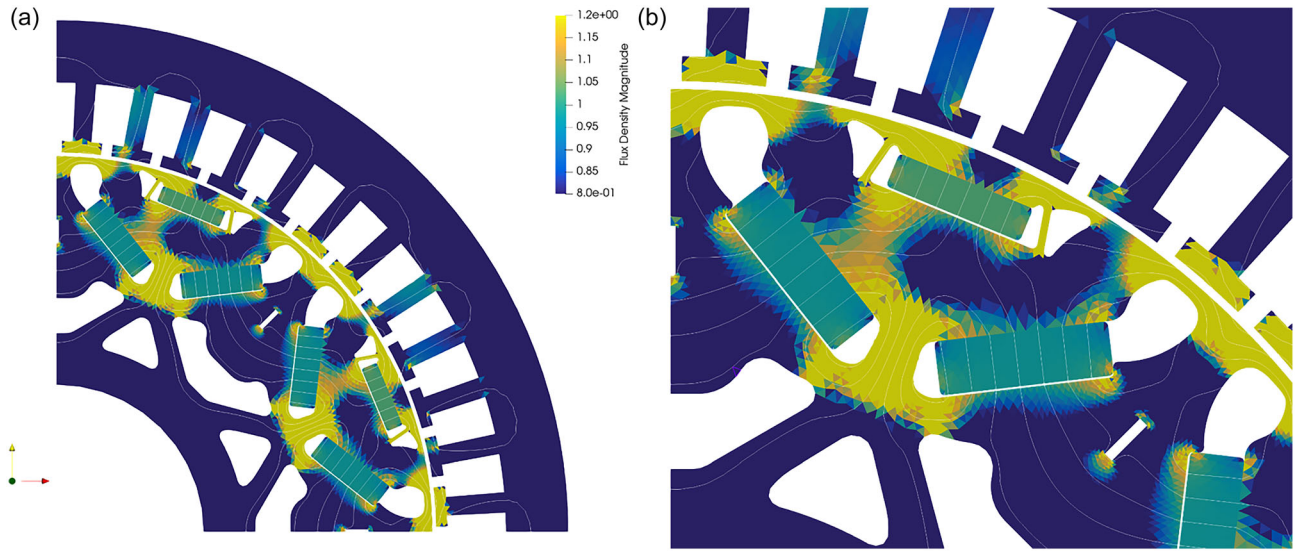

Figure 5. A 2D FE-Simulated flux density distribution for a typical internal permanent magnet synchronous traction motor from electric vehicles in the short-circuit operating point. a) overview of the geometry and b) magnified section showing that the level of demagnetization is not distributed homogenously with the highest demagnetization occurring at the edges of the inner magnets.

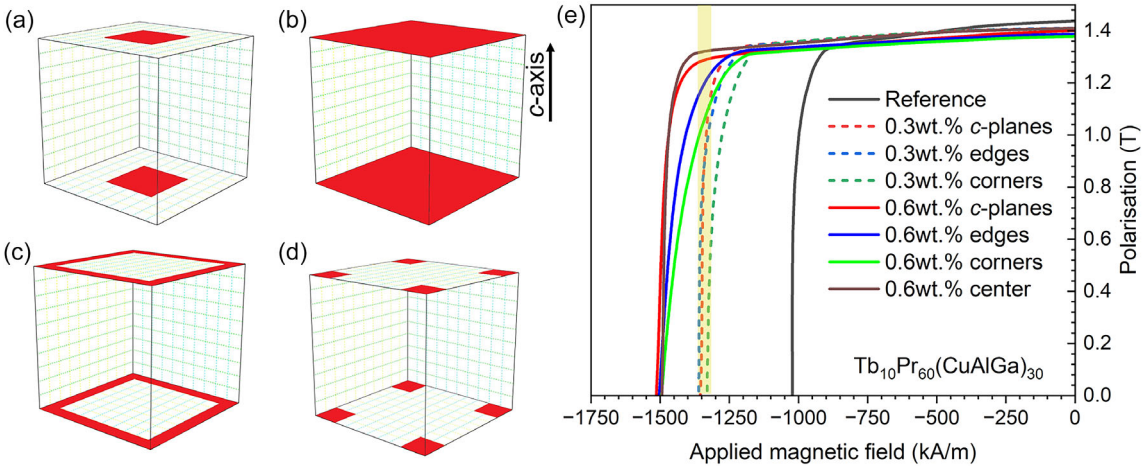

Figure 6. Sketch illustrating HRE application at different locations of the magnet: a) middle of *c*-planes, b) uniform *c*-planes, c) edges, and d) corners. The corresponding demagnetization curves after GBDP of 0.3 wt% and 0.6 wt% of $Tb_{10}Pr_{60}(Cu,Al,Ga)_{30}$ are shown in e). The shaded area in (e) indicates the statistical deviation in coercivity ($\pm 50\ kA\ m^{-1}$) after preparation and characterization of multiple samples.

It has to be noted that GBDP efficiency depends strongly on the initial sintered magnet. A different commercial grade magnet with a grain size of 5 µm (in contrast to 8.3 µm grain size for the magnet used in the rest of this work) shows larger coercivity enhancement, from up 1100 to 1990 $kA\ m^{-1}$ for the same HRE amount. Remanence remains nearly unchanged, considering the spread in the initial commercial magnets properties, which is illustrated by the shaded range. The obtained J_r and H_c values are plotted as a function of GBDP alloy and Tb amount in Figure 4b and listed in the Table S1, Supporting Information. Minimal J_r reduction is observed considering the error bar, on average, from around 1.43 to 1.41 T. The most important observation is that at first (0.3 wt%), significant H_c enhancement is achieved with minimal HRE usage. This results in a remarkable coercivity enhancement of 3866 kA/m/wt% Tb (4.86 T/wt% Tb) for 0.6 wt% GBDP alloy, which is far superior to the conventionally used TbH_x and demonstrates the potential for using multi-component grain boundary diffusion sources in production of sustainable high-performance magnets. The slope decreases for higher amounts and most likely would reach a plato at the far-right side. This implies that after reaching a certain threshold, the magnetic hardening and further HRE utilization become less efficient. A possible explanation is that the exchange length for $Nd_2Fe_{14}B$ is only few a nm and thus decoupling of adjacent grains can be achieved with little amount of grain boundary diffusion. The subsequently introduced HRE diffuses into the matrix grains, forming a thick $(Nd,Tb)_2Fe_{14}B$ shell (see SEM image in Figure 7), which therefore leads to comparably low further improvement in coercivity.

In addition, an attempt was made to enhance coercivity without using HRE by replacing Tb with Pr, resulting in $Pr_{0.7}(CuAlGa)_{0.3}$ GBDP alloy composition. In this case, a 227 $kA\ m^{-1}$ H_c enhancement was obtained.

2.3. Local Strategic Magnetic Hardening

The results in the foregoing section described HRE diffusion source optimization when applied to the top and bottom *c*-planes of the magnets. As next, a strategy to improve the HRE utilization by selective application targeting specific parts of the magnet that are most susceptible to demagnetization is presented. Finite element (FE) simulation was used for modeling the spatial distribution of magnetization and demagnetization field configuration. Detailed information about the model can be found in the supplementary information. Permanent magnet synchronous motors used for traction drives typically have to cover a large rotor speed operating range. The rotating magnetic flux generated by the permanent magnets is linked to the stator and therefore induces a voltage in the stator winding, which is proportional to the rotor speed. Due to the large speed range, the induced voltage is usually higher than the maximum voltage provided by the supplying inverter. As a result, the stator currents have to be controlled in such a way that the stator windings produce a magnetic field opposed to the rotor magnetization above a certain rotor speed level. This operation region is called the field weakening region. Aside from the intended field weakening to limit the induced voltage, field weakening can also occur unintentionally due to transient or short-circuit stator currents. As an example, to illustrate the demagnetization caused by field weakening, a typical internal permanent magnet synchronous traction

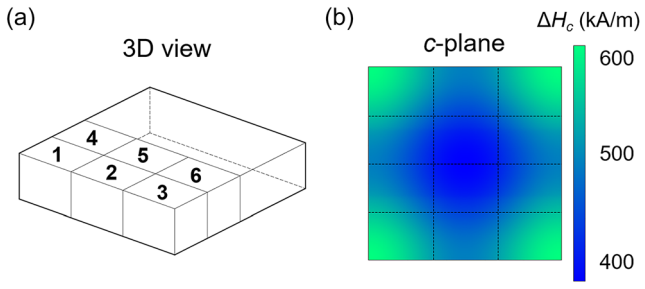

Figure 7. Sketch illustrating coercivity mapping after HRE application on *c*-planes corners. a) 3D view shows cutting in six cubes for individual local $M(H)$ measurements. b) Color map represents the resultant coercivity enhancement (ΔH_c) mapping constructed from individual measurements illustrated in (a).

Table 1. Coercivity mapping for 0.6 wt% $Tb_{10}Pr_{60}(Cu,Al,Ga)_{30}$ and TbH_x HRE sources applied on *c*-plane corners as shown in Figure 6.

Position	$Tb_{10}Pr_{60}(Cu,Al,Ga)_{30}$ H_c [kA m^{-1}]	ΔH_c [kA m^{-1}]	TbH_x H_c [kA m^{-1}]	ΔH_c [kA m^{-1}]
1	1598	587	1365	354
2	1521	510	1136	125
3	1592	581	1316	305
4	1503	492	1149	138
5	1441	430	1079	68
6	1486	475	1120	109
Average	1513	502	1210	199
Initial	1011	–	1011	–

motor for electric vehicles (EVs) is chosen. In this design, magnets are embedded in the soft magnetic rotor core. Each magnetic pole of the rotor consists of three magnets: a pair of larger magnets forming a V-shape and an additional smaller magnet closer to the rotor surface. A typical worst-case demagnetizing scenario is the so called ideal short-circuit operating point, where the rotor flux linked to the stator is zero. A 2D FE-simulation of this operating point is shown in **Figure 5**a. Here, the flux lines and the flux density amplitude are shown. In order to visualize the flux density distribution inside the magnets, the color value range has to be limited. Thus, the maximum flux density in the soft magnetic parts, which is not of interest here, is not depictable. It can be seen that due to the opposing field generated by the stator windings, there is almost no magnetic flux linkage between rotor and stator, i.e., the induced voltage is zero.

A detailed view of the flux density inside the magnets is shown in Figure 5b. Due to stray flux inside the rotor core, the magnets themselves are not completely demagnetized. The level of demagnetization is not distributed homogenously: the highest demagnetization occurs on the edges of the lower magnets, where the flux density is reduced to ≈0.8 T. Yet in large inner areas of these magnets, the flux density is only reduced to ≈1 T. Further, the smaller magnets closer to the rotor surface are less demagnetized compared to the two larger magnets. The position dependency is similar to the larger magnets, but

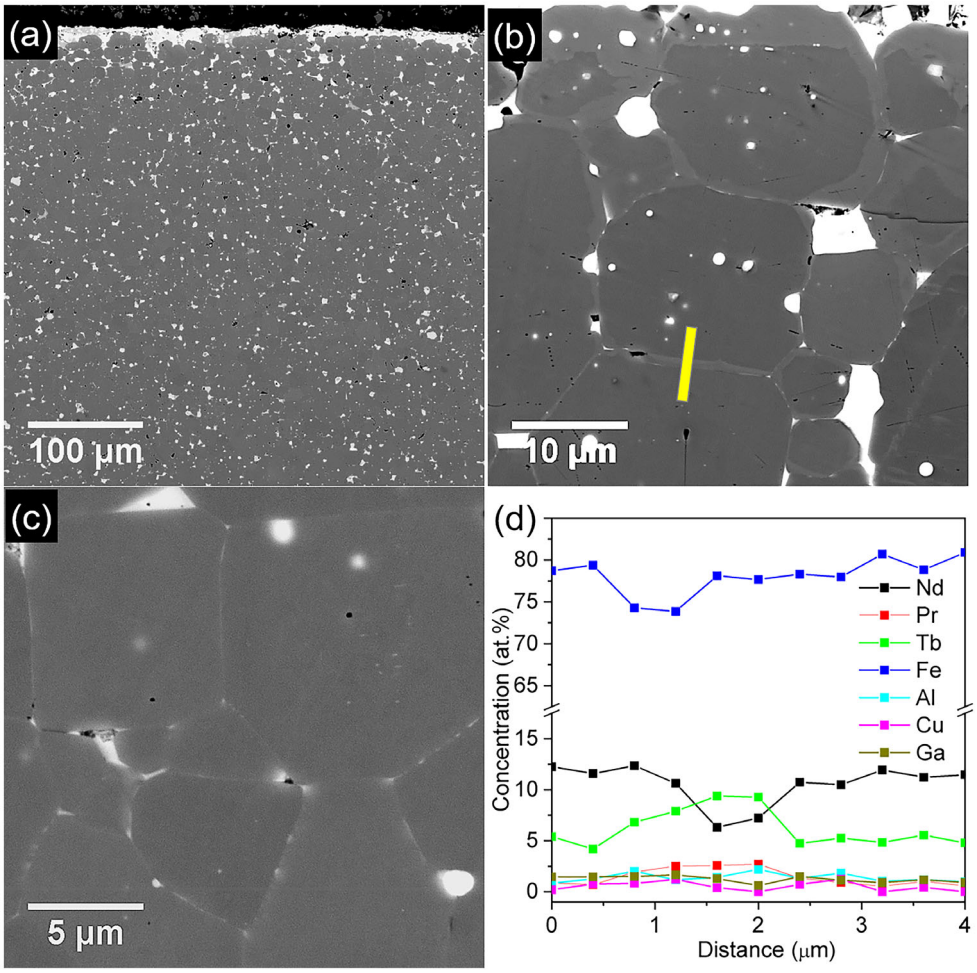

Figure 8. SEM BSE images and EDX elemental composition line scan for a GBDP sample with 0.6 wt% of $Tb_{10}Pr_{60}(Cu,Al,Ga)_{30}$ applied on corners. a) Overview showing the residual GBDP alloy on the surface, b) an area near surface with pronounced core-shell structure, c) an area in the middle part of the magnet away from the diffusion source showing no core-shell structure, and d) EDX elemental line scan across the Tb-rich shell as indicated in (b).

less pronounced regarding the amplitudes. Therefore, hardening the areas in the magnet where the highest demagnetization occurs[47,48] is a viable strategy for saving HRE[49] and can be used for the production of magnets with predefined properties in a given region.[50]

For this reason, we have studied different GBDP source application areas as shown in **Figure 6**b–d. 0.3 wt% and 0.6 wt% $Tb_{10}Pr_{60}(Cu,Al,Ga)_{30}$ melt-spun ribbons were applied a) on the middle of top and bottom *c*-planes, b) uniformly covering *c*-planes, c) edges, and d) corners. The resultant demagnetization curves in Figure 6e do not suggest significant differences for 0.3 wt%, all the samples show comparable coercivity increase after GBDP treatment. Due to the low-melting point, the diffusion alloy becomes liquid during the heat treatment and diffuses over the entire application area. In the case of 0.6 wt%, slightly better performance is observed for uniform *c*-planes and middle GBDP application. However, this could also partially result from increased ribbons layer thickness due to the limited area available on corners and edges, as well as spreading over the edges onto the side surfaces.

To shed light on the HRE diffusion and local magnetic hardening, spatial coercivity mapping was done for 0.6 wt% $Tb_{10}Pr_{60}(Cu,Al,Ga)_{30}$ and TbH_x HRE sources applied on corners (Figure 6d). $3.1 \times 10 \times 10$ mm magnet after GBDP treatment was sliced perpendicular to *c*-axis and the top layer with a thickness of about 3.1 mm was cut into smaller rectangular regions as shown in **Figure 7**. Each obtained piece was measured separately to investigate the local coercivity enhancement. The results are summarized in **Table 1** and graphically illustrated in Figure 7. Corners (1 and 3) clearly show the highest coercivity reaching nearly 1600 kA/m corresponding to 587 kA m^{-1} enhancement compared to the initial magnet. As expected for a diffusion-governed process, coercivity decrease is proportional to the distance from the diffusion source (corners), resulting in a slight decrease for sample 2 and a significant decrease for sample 5. Coercivity enhancement of the entire sample is 513 kA m^{-1}. As expected, the results are far worse for TbH_x diffusion, where ΔH_c reaches only 354 kA m^{-1} at the corners, drops more than twice, to 125 kA m^{-1} in between, and 5 times, to 68 kA m^{-1}, further away for sample number 5. These results show that for TbH_x, not only is the HRE utilization less efficient, but also the diffusion is more sluggish, resulting in shorter diffusion depth for conventional HRE sources.[9] TbH_x does not melt during the heat treatment, therefore diffusion is too slow, and it is not reaching the center of the magnet.

SEM BSE images and EDX elemental composition line scan for a GBDP sample with 0.6 wt% of $Tb_{10}Pr_{60}(Cu,Al,Ga)_{30}$ applied on corners are shown in **Figure 8**. a) Low-magnification overview shows thin residual GBDP alloy on the sample surface with a thickness under 20 µm. b) Area near the surface, right below the residual diffusion source layer, is represented by a pronounced core-shell structure . The thickness of the Tb-rich shell reaches several µm close to the GBDP alloy application and decreases gradually with distance inside the magnet. c) Area in the middle part of the magnet, away from the diffusion source shows no core-shell structure and looks similar to an untreated magnet. d) EDX elemental line scan across the Tb-rich shell reveals a reduction in Nd and an increase in Tb. In addition, a slight enhancement of Pr and Al is visible.

Scanning transmission electron microscopy-energy-dispersive X-ray spectroscopy (STEM-EDS) elemental maps for different elements near the magnet surface (area in Figure 8b) where GBDP alloy was applied are shown in **Figure 9**. RE oxides $(Nd, Pr, Tb)_x$ can be identified along with metallic Nd, and Nd–Cu and Nd–Ga-rich phases at the triple junctions. We have used the STEM-EDS line profile to evaluate the rare-earth content

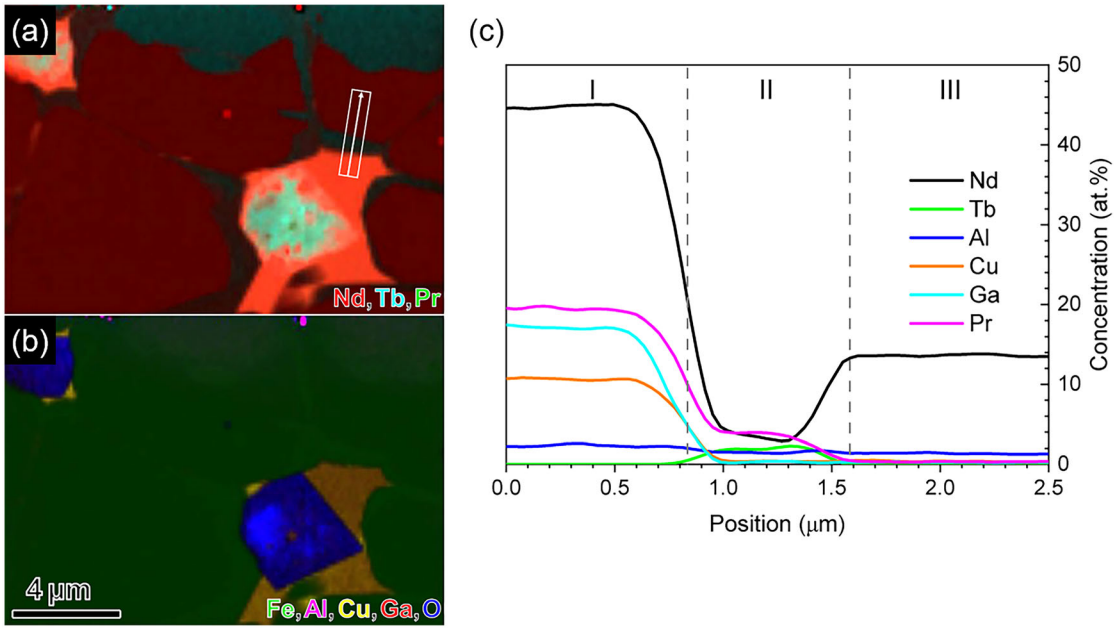

Figure 9. STEM-EDS elemental maps for a) Nd, Tb, Pr and b) Fe, Al, Cu, Ga, O. Elemental concentrations line profiles across the indicated arrow are presented in c).

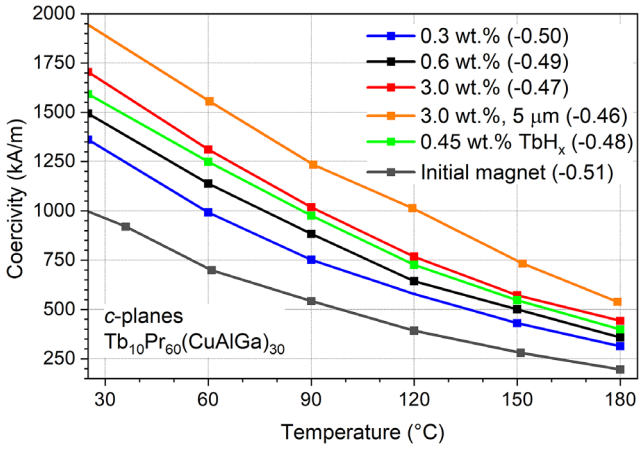

Figure 10. Temperature stability of coercivity for different GBDP sources applied on *c*-planes. The respective β values are given in the parentheses.

in the shell region since it mainly defines the local magnetic anisotropy field at the interfaces. Three regions can be distinguished from the elemental concentrations across the line scan indicated by the arrow and are presented in Figure 9c. The triple junction phase (I) is rich in Nd, Pr, Ga, and Cu. In the grain boundary region (II), Nd content is only about 3 at.% with 4 at.% Pr and 2 at.% Tb. Subsequently, in region (III), normal $Nd_2Fe_{14}B$ matrix concentrations are reached. Grain boundaries are enriched mainly in Tb and Pr whereas the diffused GBDP alloy elemental concentrations in the matrix region (III) are nearly zero. This explains well from the magnetic properties observed high HRE utilization efficiency since Tb is not diffusing in the main phase to a significant degree but remains at the grain boundaries and shell region of 2:14:1 grains. Ga and Al are reported to infiltrate along the grain boundary phase, improving wetting and promoting Tb diffusion.[51,52]

Since traction motors in EVs operate at elevated temperatures, we have measured the temperature dependance of coercivity up to 180 °C to compare the various GBDP sources in **Figure 10**. The respective temperature coefficient β values are given in parentheses. As expected from the room temperature $M(H)$ results shown in Figure 2b, the best performance is observed for 3.0 wt% $Tb_{10}Pr_{60}(Cu,Al,Ga)_{30}$ alloy corresponding to 0.4 wt% Tb (total amount applied on both sides). At 120 °C a coercivity of 771 kA m^{-1} is maintained, which, considering recent emphasis on lowering the operating temperatures of traction motors, can already be sufficient. For example, operating temperatures below 70 °C have been achieved in additively manufactured air-cooled electrical machine rotor for an automotive application.[53] Moreover, GBDP efficiency depends strongly on the initial sintered magnet. A different commercial grade magnet with a grain size of 5 μm shows larger coercivity enhancement for the same HRE amount, resulting in an impressive 1014 kA m^{-1} coercivity at 120 °C and 733 kA m^{-1} at 150 °C with using only 0.4 wt% Tb.

It has to be noted that completely eliminating HREs is an important strategy; however, this case demonstrates that with an acceptable HRE amount, which is comparable to trace elements added to commercial sintered magnets (e.g., Al, Cu, Ga), good high temperature performance can be reached. Dy and Tb amount optimization needs to be viewed keeping the rare earth (in)balance problem[54] in mind. This is illustrated in **Figure 11** showing rare earth elements production in tons/year as well as percentages in relation to Nd. Being very abundant, LREs Ce and La need to be significantly overproduced, which motivates the search for additional applications, such as moderate performance magnets. In contrast, only a fraction of HREs Tb and Dy are produced owing to their low abundance, only 1.82% in the case of Tb. This work has shown that balanced HRE contents comparable to those actually produced can be sufficient for the production of high-performance Nd–Fe–B magnets.

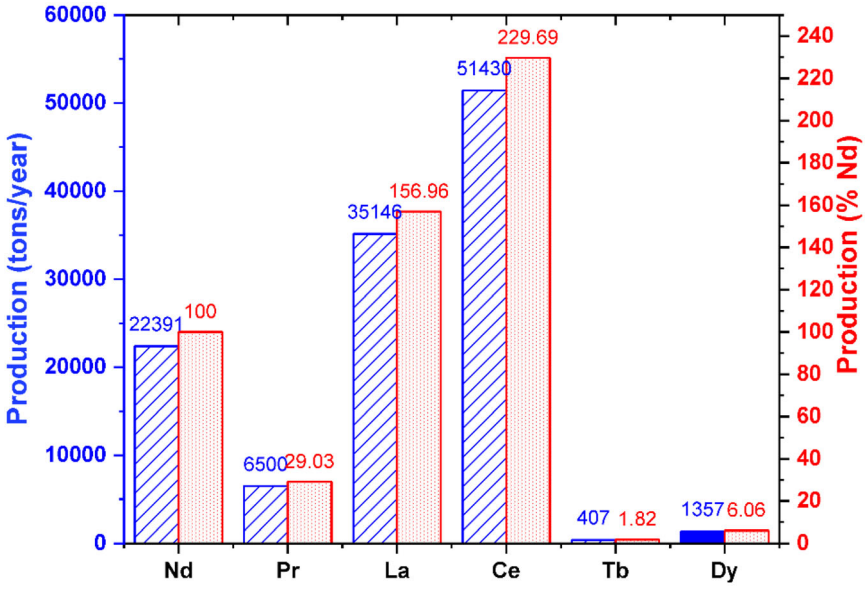

Figure 11. Production of various rare earth elements in quantity (tons/year) and relative to Nd (%).

3. Conclusion

The effects of adding a commonly industrially used GBDP HRE source, Tb hydride, as well as complex multicomponent alloys as diffusion source, on the coercivity increase of commercial grade NdFeB-based sintered magnets were investigated. Coercivity increases with powder particle size of the alloy diffusion source, reaching the highest value in the case of direct application of millimeter-size melt-spun ribbons on the magnet surface. This results in a remarkable coercivity enhancement of 3866 kA/m/wt% Tb (4.86 T/wt% Tb) for 0.6 wt% $Tb_{10}Pr_{60}(Cu, Al,Ga)_{30}$ alloy which is far superior to the conventionally used TbH_3 and demonstrates the potential for using multicomponent grain boundary diffusion sources in production of sustainable high-performance magnets. For Tb hydride, not only is the HRE utilization less efficient, but also the diffusion is more sluggish resulting in shorter diffusion depth. In addition, an attempt was made to maximize HRE utilization by selective hardening of areas in the magnet that are susceptible to demagnetization, such as corners or edges. Using FE magnetostatics simulation on an internal permanent magnet synchronous traction motor for EVs, we could show that the level of demagnetization is not distributed homogenously, with the highest demagnetization occurring at the edges and corners of the inner magnets. It would be interesting to validate the simulation results against experimental data for local demagnetization field measurements.

The work demonstrates that with a small HRE amount comparable to trace elements added to commercial sintered magnets (e.g., Al, Cu, Ga), good high temperature performance can be reached. Diffusing 0.4 wt% Tb results in coercivity of 1014 kA m^{-1} at 120 °C, showing that balanced HRE contents comparable to those actually produced can be sufficient and therefore complete elimination of HREs may not be strictly necessary.

4. Experimental Section

GBDP HRE Source Preparation: Quinary Tb or Dy containing alloys were prepared by induction melting and melt spinning (20 m s^{-1} wheel speed, 1 mm orifice, 1 mm distance from the wheel) starting from pure elements (99.99%). Prior to application, thickness of the melt-spun ribbons was measured using a micrometer ensuring reproducible and precise control over GBDP HRE source content on magnet surfaces. The induction melting was conducted under a high-purity argon atmosphere (99.999 %) after evacuating the chamber thrice to a base pressure below $5{\cdot}10^{-2}$ mbar and purging with argon. For melt spinning, the chamber was evacuated to a base pressure below $5{\cdot}10^{-5}$ mbar followed by filling with argon (99.999%). For the particle size study, the as-cast ingots were ground to powders using an agate mortar and pestle, followed by sieving to separate the respective particle size fractions (0–63; 80–163; 163–250 µm). Tb and Dy hydrides were prepared by exposing pure elements to hydrogen (100 bar, room temperature, 24 h) and subsequent jet milling (Picojet, Hosokawa Alpine). The powders were jet-milled under a high-purity argon atmosphere (99.999%) to prevent oxidation. Milling was performed with a gas pressure of 8 bar in three cycles, each separated by a 2-minute interval.

The classifier wheel speed was set up to 30 000 rpm. The particle size of the milled powders was examined by SEM and confirmed to be below 5 µm.

GBDP Experiments: Commercial-grade sintered magnets provided by VACUUMSCHMELZE GmbH & Co. KG. were used for GBDP experiments. A mixture of polyvinyl butyral (PVB) and ethanol was used as a binder to cover the targeted parts of the magnets with the HRE source. The PVB binder was first dissolved in ethanol and stirred for 30 min. A few drops of this solution were then applied onto the cleaned magnet surfaces. Subsequently, melt-spun ribbons were placed on top. The samples were left to dry in air at ambient temperature for 30 min. Mass of the initial magnet and mass of the HRE source were measured to calculate the GBDP efficiency. The samples were loaded into a quartz tube and heat treatments at 900 °C for 8 h followed by 500 °C for 4 h were done under vacuum (10^{-5} mbar) for diffusion. After the heat treatment, the samples were quenched in water under vacuum and then allowed to cool to room temperature.

Characterization: $M(H)$ measurements were carried out at a pulsed-field magnetometer from HyMPulse (Metis Instruments) in open circuit conditions. The $M(H)$ measurements were performed at 21 °C using a maximum applied magnetic field of 6.85 T. Demagnetization corrections were done according to the shape and dimensions of the samples. For each selected area of the magnets, more than 10 samples were prepared and measured. The reported coercivity values correspond to the average of these measurements with an error of ± 50 kA m^{-1}. Microstructural characterization was performed using a Tescan VEGA3-SBH SEM equipped with an Octane Plus EDS detector for elemental analysis. The composition of the samples was quantified using ICP-OES with an iCAP PRO XP Duo from Thermo Scientific, employing a standard calibration curve method. For the calibration curve, four standard solutions in the concentration range between 50 and 200 ppm for Pr, 26 and 110 ppm for Tb, 1 and 10 ppm for Dy, Co, Nb, B, and Al, and 6 and 30 ppm for Cu and Ga, as well as one blank solution, were prepared. The Fe concentration was calculated by subtracting the sum of the ppm of all measured elements from the mass of the sample. Both samples were measured twice using 50 mg of powder digested in 5 mL of 32% HCl and 1 mL of 65% HNO_3 at 210 °C for 15 min using the microwave digestion unit Ethos.lab from MLS-MWS Laboratory Solutions. For the subsequent ICP-OES analysis, the solution was diluted by a factor of 4 with 3% HNO_3. DTA for melting temperature measurements was done using DSC 404 F1 Pegasus (Netzsch). STEM was conducted using FEI Titan 80-200 with a probe aberration corrector. TEM specimens were prepared by the lift-out method using a focused ion beam system Helios G4-UX DualBeam (FEI).

Supporting Information

Supporting Information is available from the Wiley Online Library or from the author.

Acknowledgements

This work is financially supported by the Deutsche Forschungsgemeinschaft (DFG, German Research Foundation), Project ID No. 405553726, TRR 270 and by the German Ministry of Education and Research in the framework of the project "Scale2PM" (Skalierung der 2-Pulvermethode zur Herstellung von Permanentmagneten mit reduziertem Gehalt kritischer Elemente), grant number 03VP10552. A. Durgun gratefully acknowledges the financial support of the Study Abroad Postgraduate Education Scholarship (YLSY) awarded by the Republic of Türkiye Ministry of National Education. The authors thank Dr. Franziska Scheibel for conducting ICP-OES measurements as well as careful data analysis and fruitful discussions.

Open Access funding enabled and organized by Projekt DEAL.

Conflict of Interest

The authors declare no conflict of interest.

Data Availability Statement

The data that support the findings of this study are available from the corresponding author upon reasonable request.

Keywords

critical materials, diffusion, dysprosium, magnets, NdFeB, rare earth metals, terbium

Received: April 28, 2025
Revised: September 1, 2025
Published online:

[1] H. Sepehri-Amin, S. Hirosawa, K. Hono, *Handbook Of Magnetic Materials*, Elsevier **2018**, 269, https://doi.org/10.1016/bs.hmm.2018.08.003.
[2] O. Gutfleisch, M. A. Willard, E. Brück, C. H. Chen, S. G. Sankar, J. P. Liu, *Adv. Mater* **2011**, *23*, 821.
[3] S. Hirosawa, M. Nishino, S. Miyashita, *Adv. Nat. Sci: Nanosci. Nanotechnol.* **2017**, *8*, 013002.
[4] K. Hono, H. Sepehri-Amin, *Scr. Mater.* **2018**, *151*, 6.
[5] K. P. Skokov, O. Gutfleisch, *Scr. Mater.* **2018**, *154*, 289.
[6] M. Sagawa, S. Fujimura, H. Yamamoto, Y. Matsuura, S. Hirosawa, *J. Appl. Phys.* **1985**, *57*, 4094.
[7] M. Sagawa, S. Hirosawa, K. Tokuhara, H. Yamamoto, S. Fujimura, Y. Tsubokawa, R. Shimizu, *J. Appl. Phys.* **1987**, *61*, 3559.
[8] H. Nakamura, K. Hirota, M. Shimao, T. Minowa, M. Honshima, *IEEE Trans. Magn.* **2005**, *41*, 3844.
[9] T. Helbig, A. Abel, S. Sawatzki, T. Gröb, I. Dirba, S. Ener, O. Gutfleisch, *J. Alloys Compd.* **2024**, *992*, 174490.
[10] K. Loewe, D. Benke, C. Kübel, T. Lienig, K. P. Skokov, O. Gutfleisch, *Acta Mater.* **2017**, *124*, 421.
[11] H. Sepehri-Amin, T. Ohkubo, K. Hono, *Acta Mater.* **2013**, *61*, 1982.
[12] F. Li, J. Li, S. Ur Rehman, L. Zhang, Y. Hu, M. Yang, X. Yu, S. Zhong, T. Liang, *J. Alloys Compd.* **2022**, *899*, 163270.
[13] S. Lee, G. Kim, K.-S. Lee, S. Kim, T.-H. Kim, S. Lee, D.-H. Kim, W. Lee, J.-G. Lee, *Acta Mater.* **2025**, *285*, 120660.
[14] L. Zhao, J. He, W. Li, X. Liu, J. Zhang, L. Wen, Z. Zhang, J. Hu, J. Zhang, X. Liao, K. Xu, W. Fan, W. Song, H. Yu, X. Zhong, Z. Liu, X. Zhang, *Adv. Funct. Mater.* **2022**, *32*, 2109529.
[15] M. Honshima, K. Ohashi, *JMEP* **1994**, *3*, 218.
[16] I. Dirba, P. Pattur, I. Soldatov, E. Adabifiroozjaei, L. Molina-Luna, O. Gutfleisch, *J. Alloys Compd.* **2023**, *930*, 167411.
[17] S.-E. Park, T.-H. Kim, S.-R. Lee, S. Namkung, T.-S. Jang, *J. Appl. Phys.* **2012**, *111*, 07A707.
[18] J. Zuo, D. Zhang, M. Zhu, Z. Deng, X. Song, X. Wu, Z. Li, *J. Alloys Compd.* **2024**, *1005*, 176047.
[19] Y. Zhao, R. Han, X. Duan, A. Li, H. Chen, S. Dong, H. Feng, M. Zhu, G. C. Hadjipanayis, W. Li, *J. Alloys Compd.* **2024**, *1002*, 174588.
[20] M. Zhu, R. Han, W. Li, S. Huang, D. Zheng, L. Song, X. Shi, *IEEE Trans. Magn.* **2015**, *51*, 1.
[21] W. Fu, S. Guo, C. Lin, R. Chen, X. Liu, D. Lee, A. Yan, *IEEE Trans. Magn.* **2013**, *49*, 3258.
[22] K. Opelt, T. Ahmad, O. Diehl, M. Schönfeldt, E. Brouwer, I. Vogel, J. D. Rossa, J. Gassmann, S. Ener, O. Gutfleisch, *Adv. Eng. Mater.* **2021**, *23*, 2100459.
[23] T. Helbig, K. Loewe, S. Sawatzki, M. Yi, B.-X. Xu, O. Gutfleisch, *Acta Mater.* **2017**, *127*, 498.
[24] K. Opelt, C.-C. Lin, M. Schönfeldt, J. Gassmann, S. Yoon, O. Gutfleisch, *Acta Materialia* **2024**, *270*, 119871.
[25] Z. Jia, Y.-H. Li, X.-T. Yang, S. Cao, G.-F. Ding, S. Guo, X.-D. Fan, Y.-H. Xie, Z.-W. Xiong, R.-J. Chen, A.-R. Yan, *Rare Met.* **2025**, *44*, 1267.
[26] C. Lin, K. Opelt, J. D. Rossa, F. Maccari, S. Yoon, J. Gassmann, O. Gutfleisch, *Adv. Eng. Mater.* **2025**, *27*, 2500054.
[27] Z. Liu, J. He, R. V. Ramanujan, *Review, Mater. Design* **2021**, *209*, 110004.
[28] W.-Q. Liu, C. Chang, M. Yue, J.-S. Yang, D.-T. Zhang, J.-X. Zhang, Y.-Q. Liu, *Rare Met.* **2017**, *36*, 718.
[29] W. Ji, W. Liu, M. Yue, D. Zhang, J. Zhang, *Physica B: Condensed Matter.* **2015**, *476*, 147.
[30] N. Watanabe, M. Itakura, N. Kuwano, D. Li, S. Suzuki, K. Machida, *Mater. Trans.* **2007**, *48*, 915.
[31] M. Soderžnik, K. Rožman, S. Kobe, P. McGuiness, *Intermetallics* **2012**, *23*, 158.
[32] S. Sawatzki, I. Dirba, L. Schultz, O. Gutfleisch, *J. Appl. Phys.* **2013**, *114*, 133902.
[33] S. Sawatzki, I. Dirba, H. Wendrock, L. Schultz, O. Gutfleisch, *J. Magn. Magn. Mater.* **2014**, *358*, 163.
[34] T.-H. Kim, T. T. Sasaki, T. Ohkubo, Y. Takada, A. Kato, Y. Kaneko, K. Hono, *Acta Mater.* **2019**, *172*, 139.
[35] N. Oono, M. Sagawa, R. Kasada, H. Matsui, A. Kimura, *J. Magn. Magn. Mater.* **2011**, *323*, 297.
[36] M. Tang, X. Bao, K. Lu, L. Sun, J. Li, X. Gao, *Scr. Mater.* **2016**, *117*, 60.
[37] K. Lu, X. Bao, M. Tang, G. Chen, X. Mu, J. Li, X. Gao, *Scr. Mater.* **2017**, *138*, 83.
[38] H. Sepehri-Amin, I. Dirba, X. Tang, T. Ohkubo, T. Schrefl, O. Gutfleisch, K. Hono, *Acta Mater.* **2019**, *175*, 276.
[39] L. Jin, Z.-H. Jin, J.-H. Zhu, G.-F. Ding, B. Zheng, S. Guo, R.-J. Chen, A.-R. Yan, X.-C. Liu, *Chin. Phys. B* **2021**, *30*, 027503.
[40] L. Liu, H. Sepehri-Amin, T. Ohkubo, M. Yano, A. Kato, T. Shoji, K. Hono, *J. Alloys Compd.* **2016**, *666*, 432.
[41] Z. H. Kautsar, H. Sepehri-Amin, X. Tang, N. Kulesh, T. T. Sasaki, T. Ohkubo, K. Hono, *J. Alloys Compd.* **2025**, *1010*, 177738.
[42] T. Wu, S. Cao, M. Kou, Y. Xie, G. Ding, S. Guo, B. Zheng, R. Chen, M. Zhong, A. Yan, *J. Alloys Compd.* **2023**, *934*, 167888.
[43] G. Chen, X. Bao, K. Lu, X. Lv, Y. Ding, M. Zhang, C. Wang, X. Gao, *J. Magn. Magn. Mater.* **2019**, *477*, 17.
[44] J. Pan, S. Cao, Y. Li, Q. Li, G. Ding, B. Zheng, S. Guo, X. Fan, R. Chen, A. Yan, *J. Alloys Compd.* **2024**, *984*, 174003.
[45] T. Zhou, J. Chen, Q. Wang, W. Pan, Q. Huang, R. Liu, M. Li, G. Xie, *J. Alloys Compd.* **2023**, *937*, 168368.
[46] S. Hirosawa, Y. Matsuura, H. Yamamoto, S. Fujimura, M. Sagawa, H. Yamauchi, *J. Appl. Phys.* **1986**, *59*, 873.
[47] J. M. D. Coey, *Engineering* **2020**, *6*, 119.
[48] W. Li, J. Cheng, X. Lu, Y. Li, D. Zhao, W. Pei, R. Pei, *AIP Adv.* **2024**, *14*, 035233.
[49] W. Zhang, Z. Wang, Y. Luo, X. Sun, X. Bai, H. Peng, W. Yan, D. Yu, *J. Magn. Magn. Mater.* **2024**, *592*, 171768.
[50] C. Huber, C. Abert, F. Bruckner, M. Groenefeld, S. Schuschnigg, I. Teliban, C. Vogler, G. Wautischer, R. Windl, D. Suess, *Sci. Rep* **2017**, *7*, 9419.
[51] R. Song, H. Feng, H. Zhao, F. Liu, *J. Magn. Magn. Mater.* **2023**, *575*, 170744.
[52] L. Jin, G. Ding, J. Zhu, Z. Jin, B. Zheng, S. Guo, R. Chen, A. Yan, X. Liu, *J. Alloys Compd.* **2021**, *870*, 159375.
[53] M. Bieber, M. Haase, F. Tasche, A. Zibart, B. Ponick, in: *2023 IEEE International Electric Machines & Drives Conference (IEMDC)*, **2023**.
[54] K. Binnemans, P. T. Jones, T. Müller, L. Yurramendi, *J. Sustain. Metall.* **2018**, *4*, 126.